

Parallel and Scalable Heat Methods for Geodesic Distance Computation

Jiong Tao, Juyong Zhang[†], *Member, IEEE*, Bailin Deng, *Member, IEEE*,
Zheng Fang, Yue Peng, and Ying He *Member, IEEE*

Abstract—In this paper, we propose a parallel and scalable approach for geodesic distance computation on triangle meshes. Our key observation is that the recovery of geodesic distance in the heat method [1] can be reformulated as an optimization of its gradients subject to integrability, which can be solved using an efficient fixed-order method that requires no linear system solving and converges quickly. Afterwards, the geodesic distance is efficiently recovered by parallel integration of the optimized gradients in breadth-first order. Moreover, we employ a similar breadth-first strategy to derive a parallel Gauss-Seidel solver for the diffusion step in the heat method. To further lower the memory consumption from gradient optimization on faces, we also propose a formulation that optimizes the projected gradients on edges, further reducing the memory footprint by about 50%. Our approach is trivially parallelizable, with a low memory footprint that grows linearly with respect to the model size. This makes it particularly suitable for handling large models. Experimental results show that it can efficiently compute geodesic distance on meshes with more than 200 million vertices on a desktop PC with 128GB RAM, outperforming the original heat method and other state-of-the-art geodesic distance solvers.

Index Terms—Heat method, heat diffusion, poisson equation, scalability, parallel algorithm, linear time complexity.



1 INTRODUCTION

GEODESIC distance is a commonly used feature of geometry shapes and has a wide range of applications in computer vision and computer graphics [2]. For example, geodesic distance is an expression-invariant representations of faces that can be used for 3D face recognition [3]. Other important applications include object segmentation and tracking [4], [5], [6], shape analysis [7] and texture mapping [8].

Many algorithms have been proposed to compute geodesic on polyhedral meshes, like fast matching and fast sweeping [9], [10], [11], the Mitchell-Mount-Papadimitriou (MMP) algorithm [12], and the Chen-Han (CH) algorithm [13]. Recently, the heat method (HM) [1], [14] is proposed to compute geodesic distances on discrete domains, such as regular grids, point clouds, triangle meshes, and tetrahedral meshes. It is based on Varadhan’s formula [15] that relates the heat kernel and geodesic distance:

$$\lim_{t \rightarrow 0} -4t \log h(t, x, y) = d^2(x, y),$$

where x, y are arbitrary pair of points on a Riemannian manifold M , t is the diffusion time, $h(t, x, y)$ and $d(x, y)$ are the heat kernel and geodesic distance respectively. The heat method is conceptually simple and elegant. Since the geodesic distance is a solution to the eikonal equation

$$\|\nabla d\| = 1, \quad (1)$$

the heat method first integrates the heat flow $\dot{u} = \Delta u$ for a short time and normalizes its gradient to derive a unit vector field \mathbf{H} that approximates the geodesic distance gradient. Afterwards, it

determines the geodesic distance by finding scalar field d whose gradient is the closest to \mathbf{H} , which simply amounts to solving a Poisson system. The heat method involves only sparse linear systems, which can be pre-factorized once and reused to solve different right-hand-sides in linear time. This feature makes it highly attractive for applications where geodesic distances are required repeatedly. However, the Cholesky factorization used in [1], [14] requires a substantial amount of computational time and memory for large meshes. As a result, the heat method does not scale well. Although we can replace the Cholesky direct solver with iterative solvers with lower memory consumption such as the Krylov space methods, these solvers can still take a larger number of iterations with long computational time.

As technological advances make computational and imaging devices more and more powerful, we can now capture and reconstruct 3D models in higher and higher resolution. Therefore, there will be a growing demand for algorithms that can efficiently handle such large-scale data. The goal of this work is to develop a scalable algorithm for computing geodesic distance on mesh surfaces. Our method follows a similar approach as the heat method, first computing approximate gradients via heat diffusion and then using them to recover the distance. Our main insight is that instead of solving the Poisson system, we can perform the second step indirectly with much better efficiency and scalability. Specifically, we first compute an integrable gradient field that is closest to the unit vector field derived from heat diffusion, then integrate this field to obtain the geodesic distance. We formulate the computation of gradient field as a convex optimization problem, which can be solved efficiently using alternating direction method of multiplies (ADMM) [16], a first-order method with fast convergence. Unlike previous ADMM solvers that optimize function variables to regularize the gradients, our formulation uses the gradients as variables, such that each step of the solver only involves a separable subproblem and is trivially parallelizable. The resulting gradient field can be efficiently integrated using a

- J. Tao, J. Zhang and Y. Peng are with School of Mathematical Sciences, University of Science and Technology of China.
- B. Deng is with School of Computer Science and Informatics, Cardiff University.
- Z. Fang, Y. He are with School of Computer Science and Engineering, Nanyang Technological University.

[†]Corresponding author. Email: juyong@ustc.edu.cn.

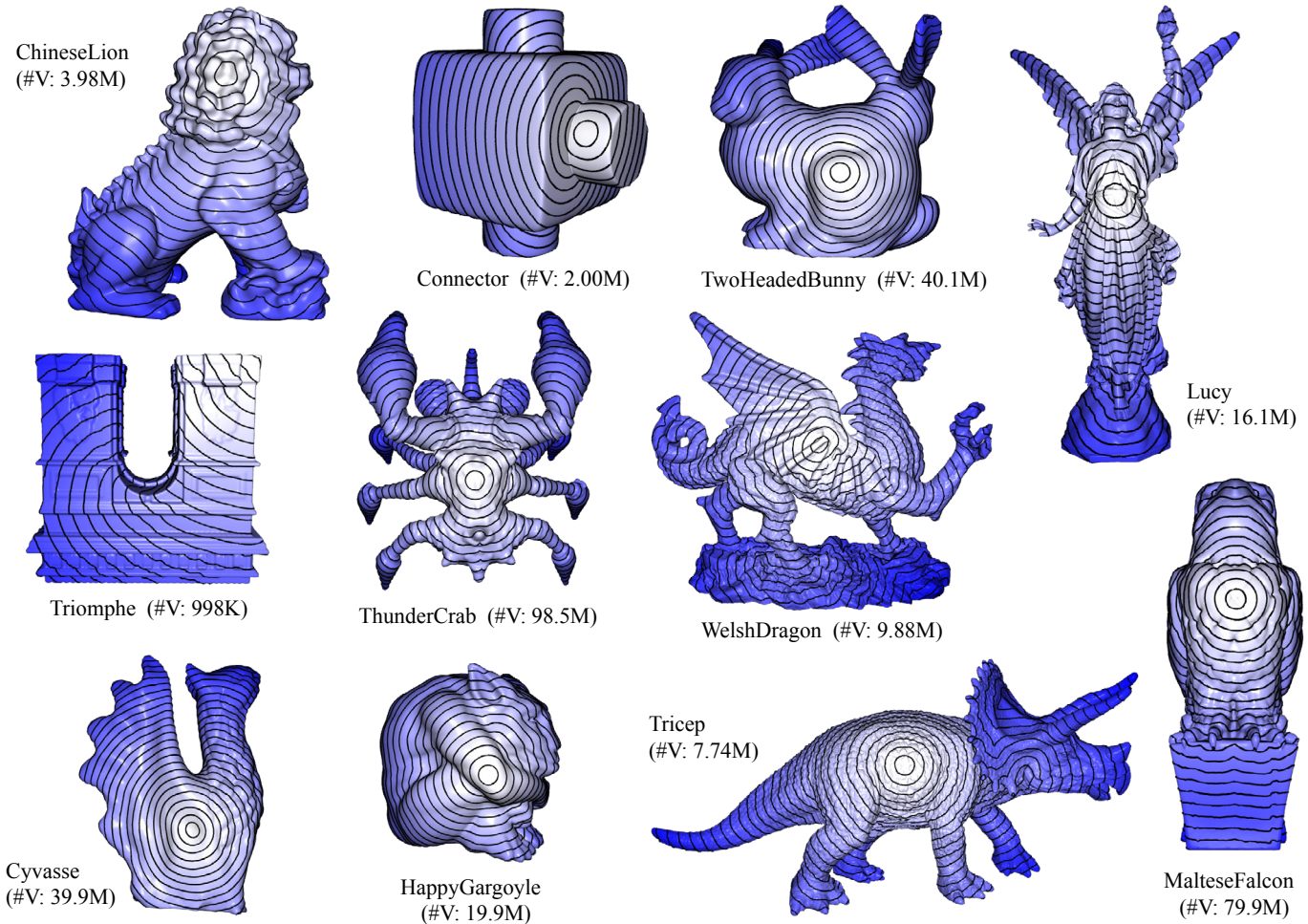


Fig. 1. Geodesic distance fields computed using our parallel and scalable heat method (Algorithm 1) on different high-resolution models, visualized using their level sets. A comparison with other methods on computational time, peak memory consumption and accuracy is provided in Tab. 1.

parallel algorithm. For the heat diffusion step, we also propose a parallel Gauss-Seidel solver, which is more efficient and robust for large meshes than direct and iterative linear solvers. The resulting method is both efficient and scalable, and can be run in parallel on multi-core processors to gain significant speedup. We evaluate the performance of our method using a variety of mesh models in different sizes. Our method significantly outperforms the original heat method while achieving similar accuracy (see Fig. 1 and Tab. 1). Moreover, the computational time and memory consumption of our approach grows linearly with the mesh size, allowing to handle much larger meshes than the heat method.

Even though our optimization approach for computing integrable gradients already provide a significant boost to the computational and memory performance compared to the original heat method, its memory footprint can be further reduced. Our key observation is that the closeness between the geodesic distance gradients and their target values can be reformulated as the closeness between their projections on the mesh edges, allowing us to formulate the problem with much fewer variables. To this end, we propose an edge-based formulation that optimizes the change of geodesic distance along the mesh edges, which we solve using a similar ADMM solver. Such changes along edges encode the directional derivatives of the geodesic distance, and the optimization result can be directly used to recover the geodesic distance by integration. Compared to the approach of computing

integrable face-based gradients, our edge-based solver can further reduce the memory footprint by about 50%. This allow us to process a model with over 200 million vertices on a desktop PC with 128GB RAM, where even the face-based optimization approach fails due to excessive memory consumption (see Fig. 8).

1.1 Our Contributions

Our main contribution is new approaches that can compute geodesic distance on mesh surfaces in an efficient and scalable way, including:

- A parallel Gauss-Seidel solver for solving short-time heat diffusion from source vertices, which is more scalable and numerically more robust than directly solving the heat diffusion linear system in [14].
- A convex optimization formulation for correcting the unit vector field derived from heat diffusion into an integrable gradient field, and an ADMM solver for solving the problem. Our solver is trivially parallelizable, and has linear time and space complexity.
- A novel edge-based formulation that optimizes the change of geodesic distance along mesh edges, which encodes the differential information of geodesic distance in a more compact way and further reduces the memory footprint compared to the face-based gradient optimization.

- An efficient parallel integration scheme to recover geodesic distance from either the face-based gradients or the edge-based changes.

2 RELATED WORK

Computing geodesic distances on discrete domains has been studied extensively in the past three decades. There are two major classes of algorithms, which are based on computational geometry and partial differential equation (PDE), respectively.

Computational geometry approaches [12], [13] maintain wavefront on mesh edges and propagate it across the faces in a Dijkstra-like sweep. They work for arbitrary manifold triangle meshes and can compute exact polyhedral distances. However, they are too computationally expensive to apply for time-critical applications. Although acceleration schemes are available [17], [18], [19], [20], [21], they are difficult to implement, and cannot adapt to discrete domains other than triangle meshes.

PDE methods are much more efficient and flexible. The fast marching method (FMM) [11] directly solves the Eikonal equation by iteratively building the solution outward from the points with known/smallest distance values on regular grids and triangulated surfaces. It runs in an optimal $O(n \log n)$ time on a triangle mesh with n vertices. Weber et al. [22] developed a highly efficient parallel FMM on geometry images, which runs in $O(n)$ time. The heat method, proposed by Crane et al. [14], adopts a different strategy. Rather than solving the distances directly, it first computes a unit vector field that approximates the gradient of the geodesic distances, then integrates the gradient by solving a Poisson equation. Based on this novel strategy, heat method only needs to solve two linear systems. Belyaev and Fayolle [23] extended the normalization-integration idea to compute the general L_p distance to a 2D curve or 3D surface, and they solve the optimization problem via ADMM.

The saddle vertex graph (SVG) method [19] is a completely different approach. It first computes a sparse undirected graph G , whose edges are direct geodesic paths (which cannot be partitioned into smaller segments). Then computing single- or multi-sources geodesic distances is equivalent to find shortest paths on G , which can be solved using Dijkstra’s algorithm. Constructing the graph takes $O(nK^2 \log K)$ time and computing geodesic distances takes $O(Kn \log n)$ time, where K is the maximal degree. As a pre-computation method, SVG is efficient and the saddle vertex graph can be constructed in parallel. However, computing the distances is intrinsically sequential. Our method does not require pre-computation, and all its three steps can be implemented in parallel.

3 ALGORITHM

Given a triangle mesh $\mathcal{M} = (\mathcal{V}, \mathcal{E}, \mathcal{F})$ and a source vertex v_s , we want to compute the geodesic distance d_i from each vertex v_i to v_s by solving the eikonal equation with boundary condition $d(v_s) = 0$. The *direct* solver (e.g., the fast marching method [11]) does not scale well due to its $O(n \log n)$ time complexity. Inspired by the heat method [1], [14], we develop a gradient-based *indirect* solver for the eikonal equation.

Similar to the heat method, we first construct a unit vector $\{\mathbf{h}_i\}$ for each face f_i using short-time heat diffusion from the source vertex. Such a vector field provides good approximation to the gradient field of the geodesic distance function, but is in

ALGORITHM 1: A parallel and scalable heat method via face-based gradient optimization.

Data: $\mathcal{M} = (\mathcal{V}, \mathcal{E}, \mathcal{F})$: a manifold triangle mesh; v_s : the source vertex; t : heat diffusion time; D_{\max} : maximum iterations of heat diffusion.

Result: The geodesic distances d_i for each vertex $v_i, i \in \mathcal{V}$.

```

// Heat diffusion from source vertex
1  $\{u_i, i \in \mathcal{V}\} = \text{Diffusion}(M, v_s, t);$ 
// Gradient normalization
2  $\mathbf{H} = -\frac{\nabla u}{\|\nabla u\|};$ 
// Optimize an integrable gradient field
3  $\mathbf{G} = \text{Integrable}(M, \mathbf{H});$ 
// Recover geodesic distance
4  $\{d_i, i \in \mathcal{V}\} = \text{Recovery}(M, v_s, \mathbf{G});$ 

```

general not integrable. The geodesic distance is then computed as a scalar field whose gradient is as close to \mathbf{h}_i as possible. Different from the original heat method that computes heat diffusion and recovers geodesic distance by directly solving linear systems, we perform these steps using iterative methods: heat diffusion is done via Gauss-Seidel iteration (Section 3.1), while the geodesic distance is computed by first correcting $\{\mathbf{h}_i\}$ into an integrable field $\{\mathbf{g}_i\}$ with an ADMM solver (Section 3.2) and then integrating it from the source vertex (Section 3.2). Algorithm 1 shows the pipeline of our method. The main benefit of our approach is its scalability: both the Gauss-Seidel heat diffusion and the geodesic distance integration can be done in parallel through breadth-first traversal over the mesh surface; the correction of $\{\mathbf{h}_i\}$ is a simple convex optimization problem and computed using an ADMM solver where each step is trivially parallelizable. Moreover, both the Gauss-Seidel solver and the ADMM solver converge quickly to a solution with reasonable accuracy, resulting in much less computational time than the original heat method. Moreover, our approach has a low memory footprint that grows linearly with mesh size, allowing it to handle very large meshes while the original heat method fails on such models due to the memory consumption of matrix factorization.

To facilitate the presentation of our method, we assume in this section that M is a topological disk and there is only one source vertex. More general cases, such as meshes with arbitrary topology and multiple source vertices, will be discussed in Section 3.4.

3.1 Heat Diffusion

Following [1], [14], we compute the initial vector field $\{\mathbf{h}_i\}$ by integrating the heat flow $\dot{u} = \Delta u$ of a scalar field u for a short time t , and taking

$$\mathbf{h}_i = -\frac{\nabla u|_{f_i}}{\|\nabla u|_{f_i}\|}. \quad (2)$$

The initial value of the scalar field u is a Dirac delta function for a source vertex. Integrating the heat flow using a single backward Euler step leads to a linear system [1], [14]:

$$(\mathbf{A} - t\mathbf{L}_c)\mathbf{u} = \mathbf{u}_0, \quad (3)$$

where vector \mathbf{u} stores the value of u for each vertex, vector \mathbf{u}_0 has value 1 for the source vertex and 0 for all other vertices, \mathbf{A} is a diagonal matrix storing the area of each vertex, and \mathbf{L}_c is the cotangent Laplacian matrix. Crane et al. [1], [14] solved this sparse linear system by prefactorizing matrix $\mathbf{A} - t\mathbf{L}$ using Cholesky

decomposition. This approach works well for meshes with up to a few million vertices, but faces difficulties for larger meshes due to high memory consumption for the factorization. Alternatively, we can solve the system using Krylov subspace methods such as conjugate gradient (CG), which requires less memory and can be parallelized [24]. However, CG may require a large number of iterations to converge for large meshes, which still results in significant computational costs.

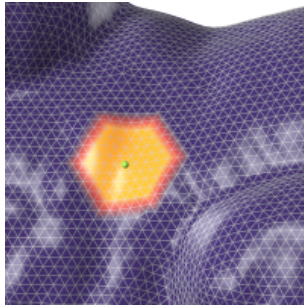
With scalability in mind, we prefer a method that can be run in parallel, without requiring many iterations to converge. Therefore, we solve the system (2) with Gauss-Seidel iteration in breadth-first order, where all vertices with the same topological distance to the source are updated in parallel. Specifically, let us define the sets

$$\begin{aligned}
 \mathcal{D}_0 &:= \{v_s\}, \\
 \mathcal{D}_1 &:= \mathcal{N}(\mathbf{D}_0) \setminus \mathcal{D}_0, \\
 \mathcal{D}_2 &:= \mathcal{N}(\mathbf{D}_1) \setminus (\mathcal{D}_0 \cup \mathcal{D}_1), \\
 &\dots \\
 \mathcal{D}_i &:= \mathcal{N}(\mathbf{D}_{i-1}) \setminus \bigcup_{k=0}^{i-1} \mathcal{D}_k,
 \end{aligned} \tag{4}$$

where $\mathcal{N}(\cdot)$ denotes the union of one-ring neighbor vertices. Intuitively, \mathcal{D}_i is the set of vertices that require at least i hops from the source v_s to reach. All such sets can be determined using breadth-first traversal of the vertices starting from v_s . Then in each outer iteration of our Gauss-Seidel solver, we update the values at vertex sets $\mathcal{D}_0, \mathcal{D}_1, \dots$ consecutively. When updating a set \mathcal{D}_i , we determine the new values for each vertex v_j from the latest values of its neighboring vertices to satisfy its corresponding equation in (3), resulting in an update rule

$$u^i(v_j) = \frac{u_0(v_j) + t \sum_{k \in \mathcal{N}_j} \theta_{j,k} u^{i-1}(v_k)}{A_{v_j} + t \sum_{k \in \mathcal{N}(j)} \theta_{j,k}}, \tag{5}$$

where A_{v_j} is the area for vertex v_j , computed as one third of the total area of triangles incident with v_j ; \mathcal{N}_j denotes the index set of neighboring vertices for v_j , $u_0(v_j)$ is the initial value of v_j , $u^{i-1}(v_k)$ is the value at v_k after the update of \mathcal{D}_{i-1} , and $\theta_{j,k}$ is the coefficient of v_k for the cotangent Laplacian at v_j . Intuitively, each outer iteration



sweeps all vertices in breadth-first order starting from the source, where all vertices at the current front are updated simultaneously using the latest values. Note that unless it is close to the source, the set \mathcal{D}_i often contains a large number of vertices. Thus the update can be easily parallelized with little overhead. An illustration figure of our heat diffusion method is shown in the inset. The green point is the source vertex, which diffuses the heat from near to far area. In current state, the vertices in the yellow part are already processed, and the heat value of vertices in the red part are being updated in parallel. In our experiments, the solver quickly converges to a solution that is good enough for the subsequent steps, significantly reducing the computational time compared with the direct solver and the Krylov subspace method. An example is provided in Fig. 2 where we show the mean error E of our solver's result in each iteration with respect to the direct

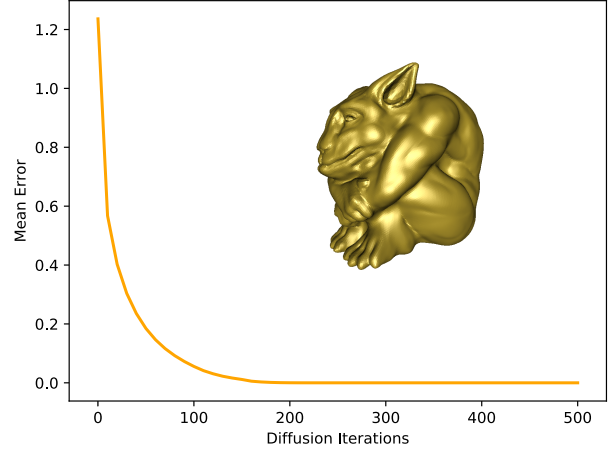


Fig. 2. Our Gauss-Seidel heat diffusion quickly decreases the mean error of the result, computed based on Eq. (6). As a result, it produces a solution good enough for subsequent steps with significantly less computational time than a direct solver or a Krylov subspace method.

solver, which is defined as

$$E = \sqrt{\frac{|\mathcal{F}|}{\sum_{i=1}^{|\mathcal{F}|} A_i} \|\mathbf{h}_i - \mathbf{h}_i^*\|^2}, \tag{6}$$

where A_i is the area of face f_i divided by the total surface area, \mathbf{h}_i is the normalized face gradient by our method, and \mathbf{h}_i^* is the normalized face gradient by directly solving Eq. (3). For this HAPPYGARGOYLE model with 63208 vertices, a direct solver for Eq. (3) takes 1.671s, while our method takes 153 iterations (0.169s) and 185 iterations (0.228s) to produce a result with mean error 1% and 0.1%, respectively.

3.2 Integrable Gradient Field

In general, the unit vector field $\{\mathbf{h}_i\}$ is not integrable. To derive geodesic distance, the heat method computes a scalar field whose gradients are as close as possible to $\{\mathbf{h}_i\}$, and shifts its values such that it becomes zero at the source vertex. This is achieved in [1], [14] by solving a Poisson linear system

$$\mathbf{L}\mathbf{d} = \mathbf{b}, \tag{7}$$

where vector \mathbf{d} stores the values of the scalar field, and \mathbf{b} stores the integrated divergence of the field $\{\mathbf{h}_i\}$ at the vertices. Similar to heat diffusion, solving this linear system using Cholesky decomposition or Krylov subspace methods will face scalability issues. Therefore, we adopt a different strategy to derive geodesic distance: we first compute an integrable gradient field $\{\mathbf{g}_i\}$ that is the closest to $\{\mathbf{h}_i\}$, and then integrate it to recover the geodesic distance. In the following, we will show that both steps can be performed using efficient and scalable algorithms.

Representing both $\{\mathbf{h}_i\}$ and $\{\mathbf{g}_i\}$ as 3D vectors, we compute $\{\mathbf{g}_i\}$ by solving a convex constrained optimization problem:

$$\min_{\{\mathbf{g}_i\}} \sum_{f_i \in \mathcal{F}} A_i \|\mathbf{g}_i - \mathbf{h}_i\|^2, \tag{8}$$

$$\text{s.t. } \bar{\mathbf{e}} \cdot (\mathbf{g}_1^e - \mathbf{g}_2^e) = 0, \quad \forall e \in \mathcal{E}_{\text{int}}, \tag{9}$$

where \mathcal{E}_{int} denotes the set of interior edges, $\bar{\mathbf{e}} \in \mathbb{R}^3$ is the unit vector for edge e , and $\mathbf{g}_1^e, \mathbf{g}_2^e$ are the gradient vectors on the two incident faces for e . The constraint (9) is a compatibility condition

that the gradient vectors on any pair of adjacent faces to have the same projection on their common edge, thus ensuring the global integrability of the vector field $\{\mathbf{g}_i\}$ on a zero-genus surface.

To solve this problem in a scalable way, we introduce for each interior edge a pair of auxiliary variables $\mathbf{y}_1^e, \mathbf{y}_2^e \in \mathbb{R}^3$ for the gradients on its adjacent faces, and reformulate the problem as

$$\min_{\{\mathbf{g}_i\}, \{\mathbf{y}_1^e, \mathbf{y}_2^e\}} \sum_{f_i \in \mathcal{F}} A_i \|\mathbf{g}_i - \mathbf{h}_i\|^2 + \sum_{e \in \mathcal{E}_{\text{int}}} \sigma_e(\mathbf{y}_1^e, \mathbf{y}_2^e) \quad (10)$$

$$\text{s.t. } \mathbf{g}_i = \mathbf{y}_k, \quad \forall f_i \in \mathcal{F}, \quad \forall \mathbf{y}_k \in \mathcal{Y}_i. \quad (11)$$

Here A_i is the face area for \mathbf{g}_i , and $\sigma_e(\cdot)$ is an indicator function for compatibility between the auxiliary gradient variables on the two incident faces of edge e :

$$\sigma_e(\mathbf{y}_1^e, \mathbf{y}_2^e) = \begin{cases} 0, & \text{if } \bar{\mathbf{e}} \cdot (\mathbf{y}_1^e - \mathbf{y}_2^e) = 0, \\ +\infty, & \text{otherwise.} \end{cases} \quad (12)$$

\mathcal{Y}_i denotes the set of auxiliary variables associated with face f_i , such that constraint (11) enforces consistency between the auxiliary variables and the actual gradient vectors. To facilitate presentation, we write it in matrix form as

$$\begin{aligned} \min_{\mathbf{G}, \mathbf{Y}} \quad & \|\mathbf{M}(\mathbf{G} - \mathbf{H})\|_F^2 + \sigma(\mathbf{Y}), \\ \text{s.t.} \quad & \mathbf{M}(\mathbf{Y} - \mathbf{S}\mathbf{G}) = \mathbf{0}. \end{aligned} \quad (13)$$

where $\mathbf{G}, \mathbf{H} \in \mathbb{R}^{|\mathcal{F}| \times 3}$ and $\mathbf{Y} \in \mathbb{R}^{2|\mathcal{E}_{\text{int}}| \times 3}$ collect the gradient variables, the input unit vector fields, and the auxiliary variables, respectively. $\sigma(\mathbf{Y})$ denotes the sum of indicator functions for auxiliary variable pairs. $\mathbf{S} \in \mathbb{R}^{2|\mathcal{E}_{\text{int}}| \times |\mathcal{F}|}$ is a selection matrix that chooses the matching gradient variable for each auxiliary variable. $\mathbf{M} \in \mathbb{R}^{2|\mathcal{E}_{\text{int}}| \times 2|\mathcal{E}_{\text{int}}|}$ is a diagonal matrix storing the square roots of face areas associated with the auxiliary variables. Introducing \mathbf{M} in the constraints does not alter the solution, but helps to make the algorithm robust to the mesh discretization. Indeed, a similar constraint reweighting strategy is employed in [25] to improve the convergence of their ADMM solver for physics simulation.

To solve this problem, ADMM searches for a saddle point of its augmented Lagrangian

$$\begin{aligned} L(\mathbf{G}, \mathbf{Y}, \boldsymbol{\lambda}) = & \|\mathbf{M}(\mathbf{G} - \mathbf{H})\|_F^2 + \sigma(\mathbf{Y}) \\ & + \text{tr} \left(\boldsymbol{\lambda}^T \mathbf{M}(\mathbf{Y} - \mathbf{S}\mathbf{G}) \right) + \frac{\mu}{2} \|\mathbf{M}(\mathbf{Y} - \mathbf{S}\mathbf{G})\|_F^2, \end{aligned}$$

where $\boldsymbol{\lambda} \in \mathbb{R}^{2|\mathcal{E}_{\text{int}}| \times 3}$ collects the dual variables, and $\mu > 0$ is a penalty parameter. The stationary point is computed iteratively, by alternating between the updates of \mathbf{Y} , \mathbf{G} , and $\boldsymbol{\lambda}$.

- **Y-update.** This step minimizes the augmented Lagrangian with respect to \mathbf{Y} , while fixing \mathbf{G} and $\boldsymbol{\lambda}$. It reduces to

$$\min_{\mathbf{Y}} \sigma(\mathbf{Y}) + \frac{\mu}{2} \left\| \mathbf{M}(\mathbf{Y} - \mathbf{S}\mathbf{G}) + \frac{\boldsymbol{\lambda}}{\mu} \right\|_F^2.$$

This is separable into a set of independent subproblems for each internal edge e :

$$\min_{\mathbf{y}_1^e, \mathbf{y}_2^e} \sigma_e(\mathbf{y}_1^e, \mathbf{y}_2^e) + \frac{\mu}{2} \sum_{i=1}^2 \left\| \alpha_i^e (\mathbf{y}_i^e - \mathbf{g}_i^e) + \frac{\boldsymbol{\lambda}_i^e}{\mu} \right\|^2,$$

where α_i^e , \mathbf{g}_i^e , $\boldsymbol{\lambda}_i^e$ ($i = 1, 2$) are the face area square root, gradient variables, and dual variables corresponding to \mathbf{y}_i^e ,

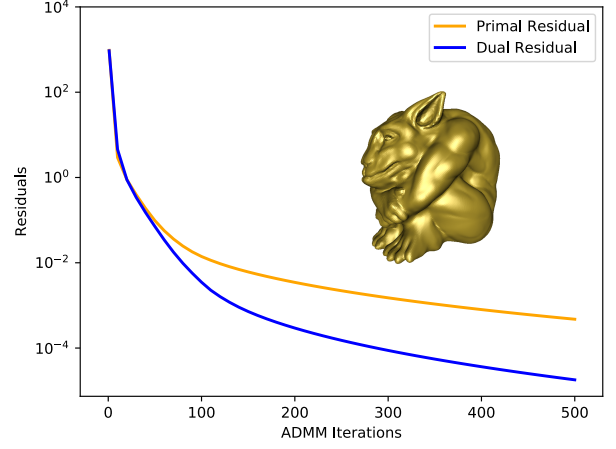


Fig. 3. The ADMM solver quickly decreases the primal and dual residuals in the initial iterations, as shown here on the same HAPPYGARGOYLE model as in Fig. 2.

respectively. This problem has a closed-form solution

$$\mathbf{y}_1^e = \mathbf{q}_1^e + \frac{A_2^e}{A_1^e + A_2^e} \bar{\mathbf{e}} (\bar{\mathbf{e}} \cdot (\mathbf{q}_2^e - \mathbf{q}_1^e)),$$

$$\mathbf{y}_2^e = \mathbf{q}_2^e - \frac{A_1^e}{A_1^e + A_2^e} \bar{\mathbf{e}} (\bar{\mathbf{e}} \cdot (\mathbf{q}_2^e - \mathbf{q}_1^e)),$$

where $\mathbf{q}_i^e = \mathbf{g}_i^e - \frac{\boldsymbol{\lambda}_i^e}{\mu \alpha_i^e}$, and A_i^e is the face area for \mathbf{y}_i^e , for $i = 1, 2$.

- **G-update.** After updating \mathbf{Y} , we fix \mathbf{Y} , $\boldsymbol{\lambda}$ and minimize the augmented Lagrangian with respect to \mathbf{G} , which reduces to independent subproblems

$$\min_{\mathbf{g}_i} A_i \|\mathbf{g}_i - \mathbf{h}_i\|^2 + \frac{\mu}{2} \sum_{\mathbf{y}_k \in \mathcal{Y}(i)} \left\| \alpha_i (\mathbf{y}_k - \mathbf{g}_i) + \frac{\boldsymbol{\lambda}_k}{\mu} \right\|^2, \quad (14)$$

where $\mathcal{Y}(i)$ denotes the set of associated auxiliary variables for \mathbf{g}_i in \mathbf{Y} , and $\boldsymbol{\lambda}_k$ denotes the corresponding components in $\boldsymbol{\lambda}$ for \mathbf{y}_k . These subproblems can be solved in parallel with closed-form solution

$$\mathbf{g}_i = \frac{2\mathbf{h}_i + \mu \sum_{\mathbf{y}_k \in \mathcal{Y}(i)} (\mathbf{y}_k + \frac{\boldsymbol{\lambda}_k}{\mu \alpha_i})}{2 + \mu |\mathcal{Y}(i)|}.$$

- **λ-update.** After the updates for \mathbf{Y} and \mathbf{G} , we compute the new values $\boldsymbol{\lambda}'$ for the dual variables as

$$\boldsymbol{\lambda}' = \boldsymbol{\lambda} + \mu \mathbf{M}(\mathbf{Y} - \mathbf{S}\mathbf{G}).$$

Convergence. Since the optimization problem (13) is convex, ADMM converges to a stationary point of the problem [16]. We measure the convergence using the primal $\mathbf{r}_{\text{primal}}$ and the dual residual \mathbf{r}_{dual} [16]:

$$\mathbf{r}_{\text{primal}} = \mathbf{M}(\mathbf{Y} - \mathbf{S}\mathbf{G}), \quad \mathbf{r}_{\text{dual}} = \mu \mathbf{A} \mathbf{S} \delta \mathbf{G},$$

where $\delta \mathbf{G}$ is the difference of \mathbf{G} between two iterations. We terminate the algorithm when both of the primal residual and dual residual are small enough, or if the iteration count exceeds a user-specified threshold I_{max} . The residual thresholds are set to $\|\mathbf{r}_{\text{primal}}\| \leq \|\mathbf{M}\|_F \cdot \epsilon_1$ and $\|\mathbf{r}_{\text{dual}}\| \leq \|\mathbf{M}\|_F \cdot \epsilon_2$, where ϵ_1, ϵ_2 are user-specified values. We set $\epsilon_1 = \epsilon_2 = 1 \cdot 10^{-5}$ in all our experiments.

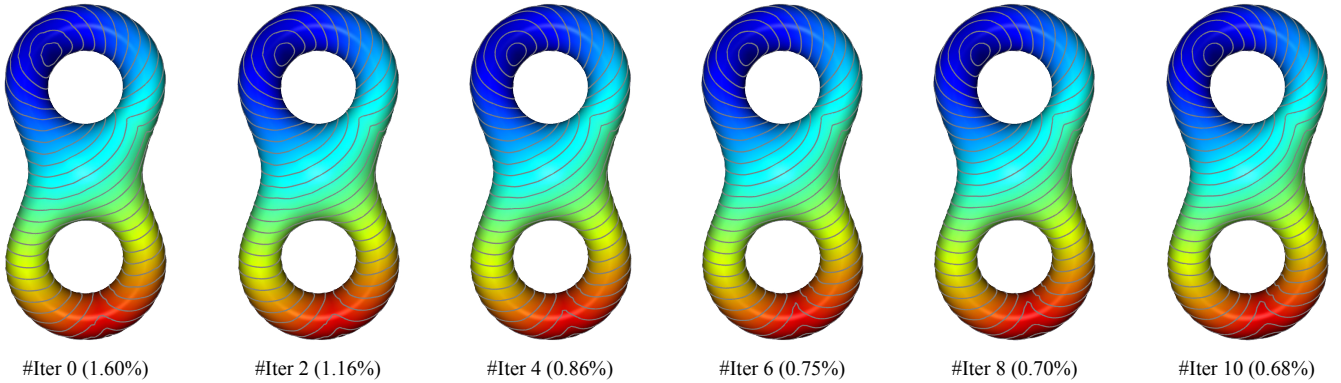


Fig. 4. Starting from the unit gradients resulting from heat diffusion, our ADMM solver can produce a geodesic distance gradient field of good accuracy within a small number of iterations. Here we run the ADMM solver for a prescribed number of iterations, and integrate the resulting gradients according to Section 3.3. The recovered geodesic distance field is visualized with color coding and level sets. The caption of each image shows the number of ADMM iterations and the mean relative error of the resulting geodesic distance, computed according to Eq. (22).

The main benefit of using ADMM is that it quickly converges to a point close to the final solution [16]. In our experiments, the algorithm only needs a small number of iterations to reduce both the primal and dual residuals to small values, as shown in Fig. 3 for the HAPPYGARGOYLE model. As a result, it only takes a small number of iterations for the ADMM solver to produce a gradient field with good accuracy compared to the exact solution (see Fig. 4 for example). Moreover, the updates of \mathbf{Y} , \mathbf{G} , and λ are all trivially parallelizable, allowing for significant speedup on multi-core processors. Finally, the memory consumption grows linearly with the mesh size, making it feasible to process very large meshes. As a result, our method is both efficient and scalable.

Remark. Our formulation using gradients as variables is a key factor in achieving efficiency and scalability for the ADMM solver. In the past, ADMM and other first-order methods have been used to solve various optimization problems that involve regularization of gradients for certain functions [26], [27], [28], [29]. These optimization problems are all formulated with the function values as the variables. For such problems, the solver typically includes a local step that updates auxiliary gradient variables according to the regularization, and a global step that updates the function variables to align with the auxiliary gradients. The global step requires solving a linear system for all the function variables, which will eventually become the bottleneck for large-scale problems. By formulating the problem using gradient variables instead, the global step of our solver reduces to a simple weighted averaging of a few auxiliary gradients, which is separable between different faces and can be done in parallel. From another perspective, the global step for a gradient optimization problem using function variables integrates the auxiliary gradients, which is globally coupled and limits parallelism. By using gradient variables, we bypass the more time-consuming global integration step, and postpone it to a later stage where we recover geodesic distance from the resulting integrable gradient field.

3.3 Integration

After computing an integrable gradient field \mathbf{g}_i , we determine the geodesic distance d at each vertex by setting $d(v_s) = 0$ and integrating \mathbf{g}_i starting from the source v_s . Similar to the heat diffusion process, we determine the geodesic distance in breadth-first order, processing the vertex sets $\mathcal{D}_1, \mathcal{D}_2, \dots$ consecutively.

For a vertex $v_j \in \mathcal{D}_i$ ($i \geq 0$), its geodesic distance is determined from a neighboring vertex $v_k \in \mathcal{D}_{i-1}$ via

$$d(v_j) = d(v_k) + \frac{1}{|\mathcal{T}_{jk}|} \sum_{f_l \in \mathcal{T}_{jk}} \mathbf{g}_l \cdot (\mathbf{p}_j - \mathbf{p}_k), \quad (15)$$

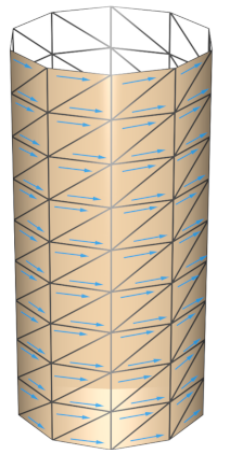
where $\mathbf{p}_j, \mathbf{p}_k \in \mathbb{R}^3$ are the positions of v_j, v_k , and \mathcal{T}_{jk} denotes the set of faces that contain both v_j and v_k . The pairing between v_j and v_k can be determined using breadth-first traversal from the source vertex. In our implementation, we pre-compute the vertex sets $\{\mathcal{D}_i\}$ as well as the vertex pairing using one run of breadth-first traversal, and reuse the information in the heat diffusion and geodesic distance integration steps. Just like our heat diffusion solver, the integration step (15) is independent between the different vertices within \mathcal{D}_i , thus can be performed in parallel with little overhead.

3.4 Extensions

Algorithm 1 is limited to genus-zero surfaces with a single source vertex. In this section, we extend it to meshes with arbitrary topology and multiple sources.

3.4.1 Complex Topology

On a surface with genus zero, the compatibility condition (9) ensures that the gradient field is globally integrable. This is no longer true for other topologies. One example is shown in the inset. For a cylindrical mesh we can construct a unit vector field that is consistently oriented along the directrix and satisfies the compatibility condition (9). This vector field is not the gradient field of a scalar function, however, because integrating along a directrix will result in a different value when coming back to the starting point. In general, for a tangent vector field on a surface of arbitrary topology to be a gradient field, we must ensure its line integral along any closed curve vanishes. On a mesh surface of genus g , such a closed curve can be generated from a cycle basis that consists of $2g$ independent non-contractible cycles [30].



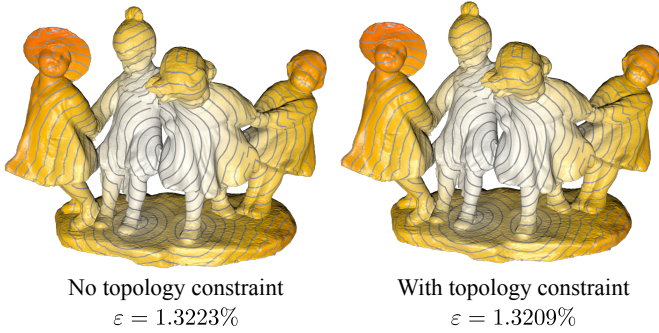


Fig. 5. Geodesic distance on a surface of genus eight, computed using Algorithm 1 with and without the topological constraint (16), and its mean relative error ε compared to the ground truth as defined in Eq. (22).

Therefore, in addition to the compatibility condition (9), we enforce an integrability condition of the field $\{\mathbf{g}_i\}$ on each cycle in the basis.

Similar to [30], we first compute a cycle basis for the dual graph of the mesh, using the tree-cotree decomposition of Eppstein [31]. Each cycle is a closed loop C of faces. Connecting the mid-points of edges that correspond to the dual edges on C , we obtain a close polyline P lying on the mesh surface, with each segment lying on one face of the loop (see inset). Then the integrability condition on this cycle can be written as

$$\sum_{f_i \in \mathcal{C}} \mathbf{g}_i \cdot \mathbf{v}_i^P = 0, \quad (16)$$

where \mathcal{C} denotes the set of faces on the cycle, and $\mathbf{v}_i^P \in \mathbb{R}^3$ is the vector of polyline segment on face f_i . Adding these conditions to the optimization problem (8)-(9), we derive a new formulation that finds a globally integrable gradient field closest to $\{\mathbf{h}_i\}$. This new problem is still convex, and can be solved similarly using ADMM.

Fig. 5 shows examples of geodesic distance on non-zero genus surfaces computed using the new formulation. The addition of global integrability conditions leads to more accurate geodesic distance, but the improvement is minor. In fact, in all our experiments, the original formulation already produces results that are close to the exact geodesic distance even for surfaces of complex topology, leaving little room of improvement. Although without a formal proof, we believe this is because the unit vector fields derived from heat diffusion are already close to the gradients of exact geodesic distance [14]. As a result, in practice the simple compatibility condition (9) is often enough to prevent pathological cases such as the cylinder example. Therefore, unless stated otherwise, all our results are generated using only constraint (9) to enforce integrability.

3.4.2 Multiple sources

Our method can be easily extended to the case of multiple sources. Following [14], we compute an initial unit vector field via heat diffusion from a generalized Dirac over the source set. This leads to a linear system with the same matrix as (3) and a different right-hand-side. Our solver for single-source heat diffusion can be easily

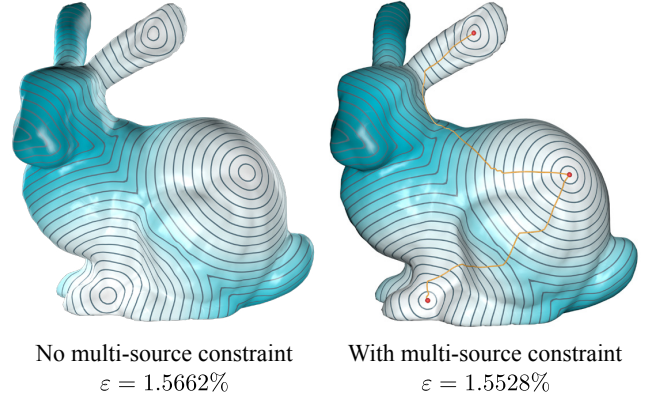


Fig. 6. Geodesic distance from multiple sources, computed using Algorithm 1 with and without the the constraint (17), and its mean relative error ε compared to the ground truth as defined in Eq. (22).

adapted to solve this linear system: we construct the breadth-first vertex sets $\{\mathcal{D}_i\}$ by including all source vertices into \mathcal{D}_0 and collecting \mathcal{D}_j ($j \geq 1$) according to the same definitions as in Eq. (4); then the Gauss-Seidel iteration proceeds exactly the same as Section 3.1. Afterwards, we find the closest integrable gradient field $\{\mathbf{g}_i\}$ and integrate it to recover the geodesic distance, in the same way as Sections 3.2 and 3.3. Strictly speaking, when computing a $\{\mathbf{g}_i\}$ we need to enforce an additional constraint: since all source vertices have the same geodesic distance, the line integral of $\{\mathbf{g}_i\}$ along any path connecting two source vertices must vanish. This can be enforced by finding a shortest edge path S from one source to each of the other sources, and introducing a constraint

$$\sum_{e_j \in S} \mathbf{e}_j \cdot \mathbf{g}_{e_j} = 0, \quad (17)$$

where e_j is an edge on the path, \mathbf{e}_j is its vector in the same orientation as the path, and \mathbf{g}_{e_j} is the gradient variable on a face adjacent to e_j . The modified formulation is still convex and can be solved using ADMM. In our experiments, however, the original formulation already produces results that are close enough to the exact solution, and the additional constraint (17) makes only limited improvement (see Fig. 6 for example). Again, this is likely due to the fact that the unit vector field derived from heat diffusion is already close to the gradients of exact geodesic distance. Moreover, our method for recovering geodesic distance from $\{\mathbf{g}_i\}$ always sets the distance at source vertices to zero, which ensures correct values at the sources even if the computed gradient field violates the constraint (17).

4 EDGE-BASED OPTIMIZATION

For the optimization formulation proposed in Section 3, the gradient variables and auxiliary variables are 3D vectors defined on faces. This can lead to redundant memory storage: since a gradient vector must be orthogonal to the face normal, it has only two degrees of freedom. This intrinsic property is disregarded by the 3D vector representations, which encode the gradients with respect to the ambient space. To reduce the memory footprint, it is possible to adopt a more compact representation, encoding a gradient vector and its associated auxiliary variables as 2D local coordinates on the face. However, this would make the compatibility conditions between two neighboring gradients more

complicated, as we must first transform the two gradients into a common local frame. This not only makes the update of auxiliary variables more involved, but also requires additional storage to encode the transformation.

In this section, we propose a new formulation for the gradient optimization problem that comes with a smaller memory footprint while maintaining the simplicity of the solver steps. The key idea is that if a face-based gradient \mathbf{g} is the same as its target value \mathbf{h} , then their projections onto the three triangle edges must be the same as well. Moreover, the inner product between the gradient \mathbf{g} and an edge vector $\mathbf{e} = \mathbf{v}_1 - \mathbf{v}_2$ encodes the change of the underlying scalar function d between its two vertices v_1 and v_2 , i.e., $\mathbf{g} \cdot \mathbf{e} = d(v_1) - d(v_2)$. Furthermore, given a non-degenerate triangle, any vector orthogonal to its normal can be uniquely recovered from the inner products between the vector and its three edge vectors. Therefore, we can encode the geodesic distance gradients $\{\mathbf{g}_i\}$ and their targets $\{\mathbf{h}_i\}$ using their inner products with their respective triangle edges. And instead of penalizing the difference between \mathbf{g}_i and \mathbf{h}_i directly, we can penalize the difference between their inner products with edge vectors.

In the following, we first present the optimization formulation and its solver based on this idea. Afterwards, we analyze its memory consumption in Section 4.2, to show that it is indeed more memory-efficient than the face-based optimization approach.

4.1 Formulation

To compute a geodesic distance function d on a triangle mesh, we define for each edge e a scalar variable x_e that represents the difference of d on its two vertices. In particular, it correspond to the change of d along one of the halfedges of e . We denote this halfedge as its *orientation halfedge* η_e . As mentioned previously, $x_e = \mathbf{g} \cdot \mathbf{e}$, where \mathbf{g} is the gradient of d on an incident faces f of e , and \mathbf{e} is the vector for the orientation halfedge η_e . Let \mathbf{h} be the target normalized gradient on f , then we can penalize the deviation between \mathbf{g} and \mathbf{h} using their squared difference along edge e , resulting in an error term $(x_e - \mathbf{h} \cdot \mathbf{e})^2$. Then the geodesic distance function across the whole mesh is computed by solving an optimization problem

$$\min_{\mathbf{X}} \quad \frac{1}{2} \sum_{e \in \mathcal{E}} \sum_{\mathbf{h} \in \mathcal{H}_e} \|x_e - \mathbf{h} \cdot \mathbf{e}\|^2, \quad (18)$$

$$\text{s.t.} \quad \sum_{k=1}^3 s_k^f \cdot x_{e_k^f} = 0, \quad \forall f \in \mathcal{F}. \quad (19)$$

Here \mathcal{E} is the set of mesh edges; \mathcal{F} is the set of mesh faces; $\mathbf{X} \in \mathbb{R}^{|\mathcal{E}|}$ collects the edge variables; \mathcal{H}_e denotes the set of target gradients on incident faces of e , such that $|\mathcal{H}_e|$ is either 1 or 2 for any edge that is not isolated. The constraint (19) is an integrability condition for the variables $\{x_e\}$, so that the total change of function d along an edge loop must vanish. Here e_1^f, e_2^f, e_3^f are the three edges incident with a face f , and $s_1^f, s_2^f, s_3^f \in \{-1, 1\}$ are their signs relative to the edge loop of f (see Figure 7 for an example). Note that for orientable 2-manifold meshes represented using halfedge data structures such as those from [32], [33], the halfedges incident with a face must form a oriented loop. In this case, the value of s_k^f ($k = 1, 2, 3$) can be easily determined from the orientation halfedge $\eta_{e_k^f}$: $s_k^f = 1$ if $\eta_{e_k^f}$ is incident with face f , otherwise $s_k^f = -1$.

To solve this optimization problem, we first introduce for each face f three auxiliary scalar variables $w_{e_1^f}, w_{e_2^f}, w_{e_3^f}$ correspond-

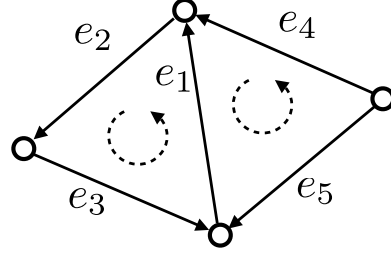


Fig. 7. The integrability condition for the edge variables within a triangle depends on the direction of their orientation halfedges, shown using arrows in this figure. The dashed arcs show the orientation for each triangle. For this particular example, the integrability condition for the two triangles are $x_{e_1} + x_{e_2} + x_{e_3} = 0$ and $-x_{e_1} + x_{e_4} - x_{e_5} = 0$, respectively.

ing to the edge variables $x_{e_1^f}, x_{e_2^f}, x_{e_3^f}$. Then we can reformulate the problem in a matrix form as

$$\begin{aligned} \min_{\mathbf{X}, \mathbf{W}} \quad & \frac{1}{2} \|\mathbf{R}\mathbf{X} - \mathbf{Z}\|^2 + \sigma(\mathbf{W}), \\ \text{s.t.} \quad & \mathbf{W} - \mathbf{R}\mathbf{X} = 0. \end{aligned}$$

Here \mathbf{X} collects all edge variables $\{x_e\}$; $\mathbf{Z} \in \mathbb{R}^{3|\mathcal{F}|}$ collects all target difference values $\mathbf{h} \cdot \mathbf{e}$ ($e \in \mathcal{E}$, $\mathbf{h} \in \mathcal{H}_e$), arranged in triplets each induced by the target gradient on a face; $\mathbf{R} \in \mathbb{R}^{3|\mathcal{F}| \times |\mathcal{E}|}$ is a sparse selection matrix that chooses the edge variables according to its target difference values; $\mathbf{W} \in \mathbb{R}^{3|\mathcal{F}|}$ collects the auxiliary variables arranged in the same order as \mathbf{Z} ; σ is an indicator function for the integrability condition (19):

$$\sigma(\mathbf{W}) = \begin{cases} 0 & \text{if } \sum_{k=1}^3 s_k^f \cdot w_{e_k^f} = 0 \quad \forall f \in \mathcal{F}, \\ +\infty & \text{otherwise.} \end{cases}$$

Similar to the face-based optimization approach, we solve this problem using ADMM. Its augmented Lagrangian function is

$$\begin{aligned} L(\mathbf{X}, \mathbf{W}, \boldsymbol{\lambda}) = & \frac{1}{2} \|\mathbf{Z} - \mathbf{R}\mathbf{X}\|^2 + \sigma(\mathbf{W}) \\ & + \boldsymbol{\lambda} \cdot (\mathbf{W} - \mathbf{R}\mathbf{X}) + \frac{\mu}{2} \|\mathbf{W} - \mathbf{R}\mathbf{X}\|^2, \end{aligned}$$

where $\boldsymbol{\lambda} \in \mathbb{R}^{3|\mathcal{F}|}$ and $\mu \in \mathbb{R}$ are the dual variables and the penalty parameter, respectively. Then ADMM finds a stationary point of the augmented Lagrangian by iterating between three steps:

- **Fix \mathbf{X} , $\boldsymbol{\lambda}$, update \mathbf{W} .** This reduces to separable subproblems for each face f :

$$\begin{aligned} \min_{\mathbf{w}_f} \quad & \left\| \mathbf{w}_f - \mathbf{x}_f + \frac{\boldsymbol{\lambda}_f}{\mu} \right\|^2 \\ \text{s.t.} \quad & \mathbf{q}_f \cdot \mathbf{w}_f = 0, \end{aligned}$$

where $\mathbf{w}_f \in \mathbb{R}^3$ are the components of \mathbf{W} corresponding to the target gradient on face f , $\mathbf{q}_f \in \{1, -1\}^3$ stores the signs for the components of \mathbf{w}_f in the integrability condition, and $\mathbf{x}_f, \boldsymbol{\lambda}_f$ are the corresponding components of \mathbf{X} and $\boldsymbol{\lambda}$ respectively. The problem has closed-form solution

$$\mathbf{w}_f = (\mathbf{I}_3 - \frac{1}{3} \mathbf{q}_f \mathbf{q}_f^T) (\mathbf{x}_f - \frac{\boldsymbol{\lambda}_f}{\mu}),$$

where \mathbf{I}_3 is the 3×3 identity matrix.

- **Fix \mathbf{W} , $\boldsymbol{\lambda}$, update \mathbf{X} .** This leads to independent subproblems

TABLE 1

Comparison of computational time (in seconds), peak memory consumption (in MB), and accuracy between VTP [21], heat method [1], variational heat method [23], and our methods (face-based and edge-based), on a PC with an octa-core CPU and 128GB memory. The accuracy is measured with the mean relative error ε defined in Eq. (22) using the VTP result as ground truth. For the heat method and its variants, we search for each model the the optimal smoothing factor m (see Eq. 21) that produce results with the best accuracy.

Model		Triomphe	Connector	ChineseLion	Tricep	WelshDragon	Lucy	HappyGargoyle	Cyvasse	TwoHeadedBunny	MalteseFalcon	ThunderCrab
Number of Vertices		997,635	2,002,322	3,979,442	7,744,320	9,884,764	16,092,674	19,860,482	39,920,642	40,103,938	79,899,650	98,527,234
VTP	Time	17.66	224.82	235.78	178.41	568.54	1320.15	5060.72	12363.21	16681.46	28309.32	22298.76
	RAM	1,218	2,502	4,849	9,664	12,394	18,670	23,464	46,976	47,258	93,127	114,610
HM	Precompute	10.22	26.17	54.69	115.97	153.34	281.97	388.87	Out of Memory			
	Solve	0.69	1.54	3.07	5.71	7.24	12.69	16.46	Out of Memory			
	RAM	2,951	6,160	12,207	23,945	30,677	51,144	65,545	Out of Memory			
	ε	0.31%	0.15%	0.73%	0.84%	1.21%	0.46%	0.29%	Out of Memory			
	m	1.0	2.3	3.1	12.6	11.1	13.0	15.7	Out of Memory			
Variational-HM	Precompute	11.7	29.34	61.31	129.07	171.24	310.01	424.81	Out of Memory			
	Solve	5.55	11.69	23.78	48.61	63.67	113.99	149.45	Out of Memory			
	RAM	3,265	6,805	13,426	26,377	33,720	56,186	71,644	Out of Memory			
	ε	0.44%	0.14%	0.52%	0.59%	0.91%	0.29%	0.21%	Out of Memory			
	m	1.0	2.3	3.4	13.4	11.8	13.9	16.6	Out of Memory			
Ours (Face)	Time	3.44	11.29	20.29	50.24	65.20	148.65	171.73	355.42	343.07	834.52	1174.45
	RAM	1,071	1,974	3,828	7,417	9,420	15,370	18,957	38,027	38,202	76,106	93,850
	ε	0.48%	0.59%	0.46%	0.50%	0.50%	0.50%	0.55%	0.86%	0.83%	0.82%	1.24%
	GS Iters	300	800	800	1000	1200	1500	2000	2000	2000	2000	2000
	m	1.0	1.0	1.0	1.0	1.0	1.0	1.0	1.0	1.0	1.0	1.0
Ours (Edge)	Time	2.06	5.60	10.13	33.37	37.32	80.15	87.86	311.33	298.25	1283.56	1657.98
	RAM	543	983	1,942	3,777	4,819	7,872	9,704	19,476	19,566	38,933	48,009
	ε	0.77%	0.81%	0.96%	0.84%	1.00%	0.86%	1.05%	0.93%	0.94%	0.94%	1.41%
	GS Iters	200	400	400	700	700	800	1000	1900	1800	4000	4000
	m	1.0	1.0	1.0	1.0	1.0	1.0	1.0	1.0	1.0	10.0	10.0

for each edge e :

$$\min_{x_e} \sum_{\mathbf{h} \in \mathcal{H}_e} (x_e - \mathbf{h} \cdot \mathbf{e})^2 + \mu (w_{\mathbf{h}}^e - x_e + \frac{\lambda_{\mathbf{h}}^e}{\mu})^2,$$

where $w_{\mathbf{h}}^e$ is the component of \mathbf{W} for edge e induced by a target gradient \mathbf{h} , and $\lambda_{\mathbf{h}}^e$ is the corresponding component of λ . It has closed-form solution

$$x_e = \frac{\sum_{\mathbf{h} \in \mathcal{H}_e} \mathbf{h} \cdot \mathbf{e} + \lambda_{\mathbf{h}}^e + \mu w_{\mathbf{h}}^e}{|\mathcal{H}_e| (1 + \mu)}. \quad (20)$$

- **Fix \mathbf{X}, \mathbf{W} , update λ .** The updated dual variables λ' are computed as

$$\lambda' = \lambda + \mu(\mathbf{W} - \mathbf{R}\mathbf{X}).$$

The convergence of the solver is indicated by small norms of the primal and dual residuals:

$$\mathbf{r}_{\text{primal}} = \mathbf{W} - \mathbf{R}\mathbf{X}, \quad \mathbf{r}_{\text{dual}} = \mu \mathbf{R} \delta \mathbf{X},$$

where $\delta \mathbf{X}$ is the difference of \mathbf{X} in two consecutive iterations.

4.2 Analysis

Compared with the face-based formulation in Section 3.2, our edge-based formulation has a much lower memory footprint. Let N_E and N_F be the number of vertices, edges, and faces in the mesh, respectively. The face-based formulation requires at least the following storage:

- For each face: two 3D vectors for the gradient variable and the target gradient, respectively.

- For each internal edge: two 3D vectors for the auxiliary gradient variables, two 3D vectors for the dual variables, and one 3D vector for the edge direction used in the \mathbf{Y} -update.

Therefore, for a mesh with no boundary, the face-based formulation requires at least a storage space of $(6N_F + 15N_E) \cdot M$ bytes, where M is the width of a floating point value. Accordingly, the edge-based formulation requires the following storage:

- For each edge: one scalar variable for the change of geodesic distance along the edge, and one scalar for pre-computed value $\sum_{\mathbf{h} \in \mathcal{H}_e}$ used in the update equation (20).
- For each face: three scalars for auxiliary variables, three flags of their signs in the integrability condition, and three scalars for the dual variables.

Thus the edge-based formulation requires storage of $(6N_F + 2N_E) \cdot M + 3N_F \cdot K$ bytes, where K is the width of a sign flag. As the sign only takes two possible values, we can store it with as little storage as a single bit. Even if we store it using an integral data type, we can still ensure $K \leq M/2$. Moreover, for a mesh without boundary, we have $N_E = \frac{3}{2}N_F$. Thus the edge-based formulation can at least reduce the storage by $12N_E \cdot M$ bytes, which can be significant for large models. In our experiments, a solver using our edge-based formulation can reduce the peak memory consumption by about 50% compared to a face-based solver. Detailed comparison is provided in Table 1.

5 EXPERIMENTAL RESULTS & DISCUSSIONS

We implement our algorithm in C++ and use OpenMP for parallelization. The source code is available at <https://github.com/bldeng/ParaHeat>. Following [1], we set the heat diffusion time as

$$t = m \cdot h^2, \quad (21)$$

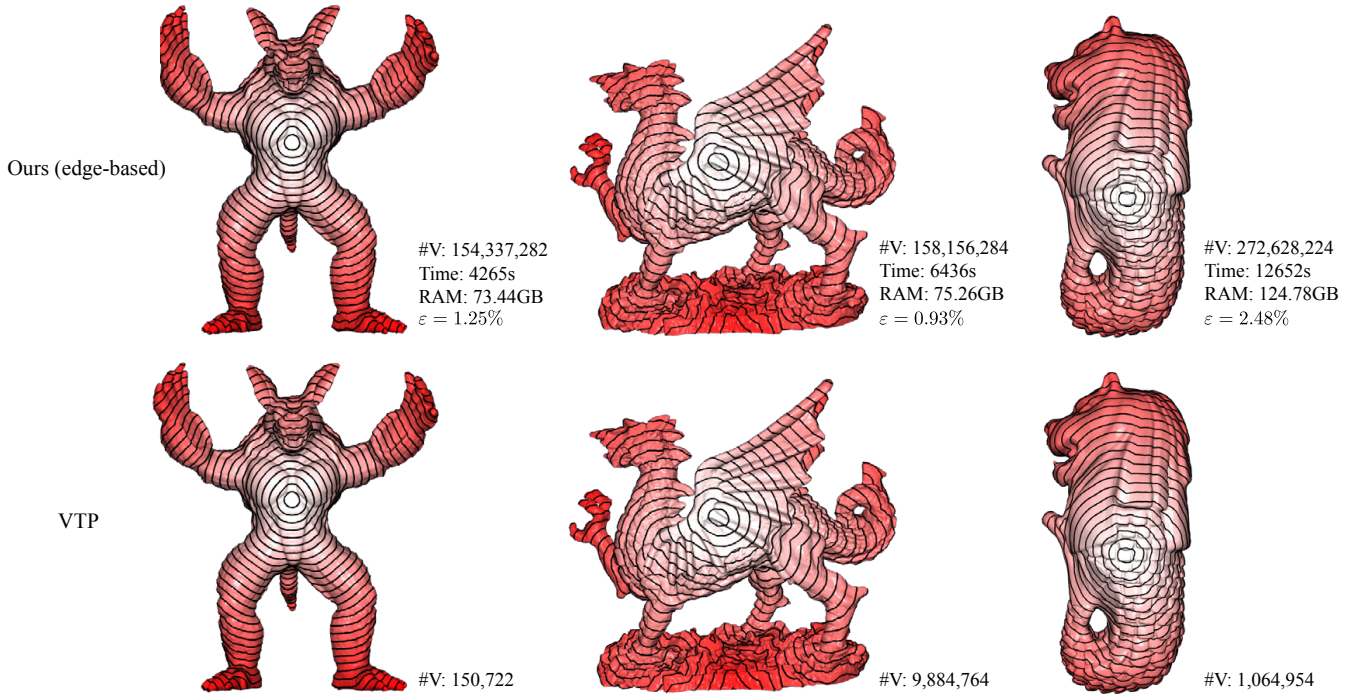


Fig. 8. We repeatedly subdivide some meshes (bottom row) to obtain very high-resolution models (top row). On such models, even our face-based method runs out of memory, while our edge-based method can still work on a PC with 128GB RAM and a octa-core CPU at 3.6 GHz. The numbers on the top row show the performance and accuracy of our edge-based method on each model. The bottom row shows the VTP results on the original models for comparison.

where h is the average edge length and m is a smoothing factor. In our experiments, setting m to a value between 1 and 10 leads to good results. For the maximal iteration of the ADMM solver I_{\max} , we observe a good balance between speed and accuracy by setting $I_{\max} = 10$, and use it as the setting in all our experiments.

5.1 Performance Comparison

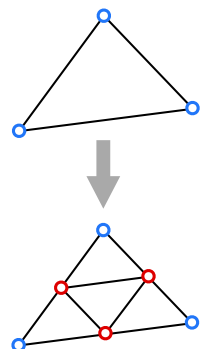
In the following, we evaluate the performance of our algorithm (including the face-based method and edge-based method), and compare it with the state-of-the-art methods, including the original heat method (HM) with Cholesky decomposition [1], the variational heat method (Variational-HM) [23], and the VTP method [19]. Tab. 1 reports the running time, peak memory consumption and accuracy of each method, for the models in Fig. 1. All examples are run on a desktop PC with an Intel Core i7 octa-core CPU at 3.6GHz and 128GB of RAM. For the original heat method, we show its pre-computation time for matrix factorization and the solving time for back substitution separately. For our method, we show the computational time using eight threads. For a fair comparison, for both HM and Variational-HM the linear system matrix factorization is done using the MA87 routine from the HSL library [34], which is a multicore sparse Cholesky factorization method [35]. Following [17], we measure the accuracy of each method using its mean relative error ϵ defined as

$$\epsilon = \frac{1}{|\mathcal{V}|} \sum_{v \in \mathcal{V} \setminus \mathcal{S}} \frac{|d(v) - d^*(v)|}{|d^*(v)|}, \quad (22)$$

where \mathcal{V} is the set of mesh vertices, \mathcal{S} is the set of source vertices, and $d^*(v), d(v)$ are the ground truth geodesic distance and the distance computed by the method at vertex v , respectively. Since VTP computes the exact geodesic distance, we use its result

as the ground truth. From Tab. 1 we can see that our methods consume less memory than all other methods, and take the least computational time while achieving similar accuracy as the heat method. The difference is the most notable on the largest models with more than 39 million vertices: both the heat method and the variational heat method run out of memory, while our methods are more than an order of magnitude faster than VTP and produce results with mean relative error no more than 1.41%. Between our two approaches, the edge-based method consumes about 50% less memory than the face-based method.

To further verify the memory efficiency of our edge-based method, we apply it to models with even higher resolution than those in Tab. 1. One challenge for such tests is to measure the accuracy, because VTP will also run out of memory on such models and cannot provide the ground truth. To overcome this problem, we take some high-resolution meshes where VTP is applicable, and repeatedly subdivide them to increase their resolution. Each subdivision step splits each triangle into four triangles, by adding a new vertex at the mid point of each edge and then connecting these new vertices, as shown in the inset. Note that such operation does not alter the metric on the mesh surface, as the four new triangles coincide with the original triangle. Therefore, if we take a vertex v_s that exists in the initial mesh \mathcal{M}^0 as the source vertex, then for any other vertex v that also exists in \mathcal{M}^0 , their geodesic distance on the initial mesh and on a subdivided mesh has the same value. Therefore, to measure the accuracy, we select a vertex from \mathcal{M}^0 as the source to compute the geodesic distance on the subdivided



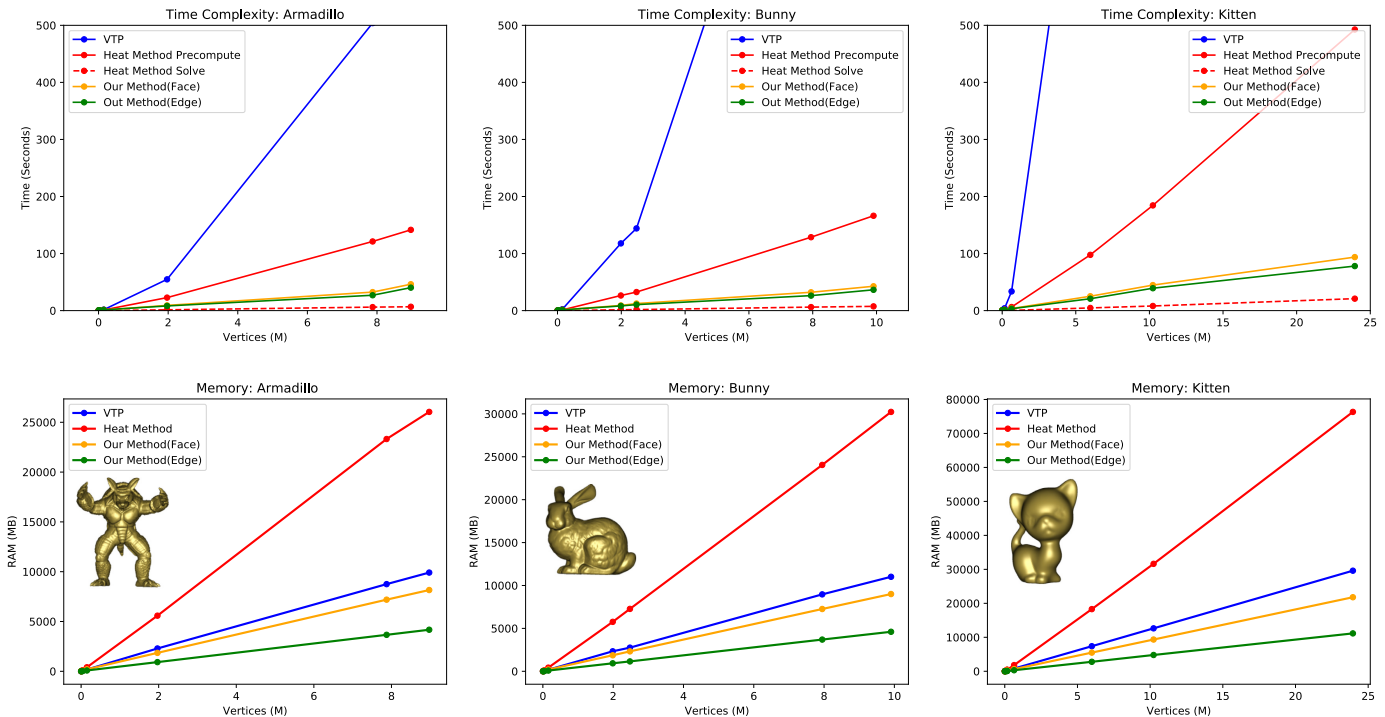


Fig. 9. Time and space complexity. We show how the computation time (the first row) and peak memory consumption (the second row) change along with different mesh resolutions on three test models. We show the results of our method, VTP [21], heat method [1] and variational heat method [23].

mesh, and evaluate its mean relative error using only the vertices that exist in the initial mesh, with the VTP solution on \mathcal{M}^0 as the ground truth. Fig. 8 shows some examples of such models, where even our face-based method runs out of memory, while our edge-based method can produce results with good accuracy.

5.2 Space and Time Complexity

Fig. 9 compares the growth of computational time and peak memory consumption between VTP, the original heat method, and our methods, on meshes with the same underlying geometry in different resolutions. The graphs verify the $O(n^2)$ time complexity of VTP as well as the fast growth of memory footprint for the original heat method, which cause scalability issues for both methods. In comparison, our methods achieve near linear growth in both computational time and peak memory consumption, allowing them to handle much larger meshes.

5.3 Parallelization

To evaluate the speedup of the parallel version, we re-run our face-based method on the same model using one, two, four and eight threads, respectively. We fix the Gauss-Seidel iteration count to 600 in the experiments. Fig. 10 shows the timing and the percentage of different steps within the total time. We observe that the ratio of the running time for each step is roughly the same with different numbers of threads, and the total computational is almost inversely proportional to the number of threads. This indicates a high level of parallelism and low overhead of our method, which scales well with the number of processors. The parallelization test is run on our face based method, and our edge based method can also achieve high level of parallelism due to the same algorithm principle between the two methods.

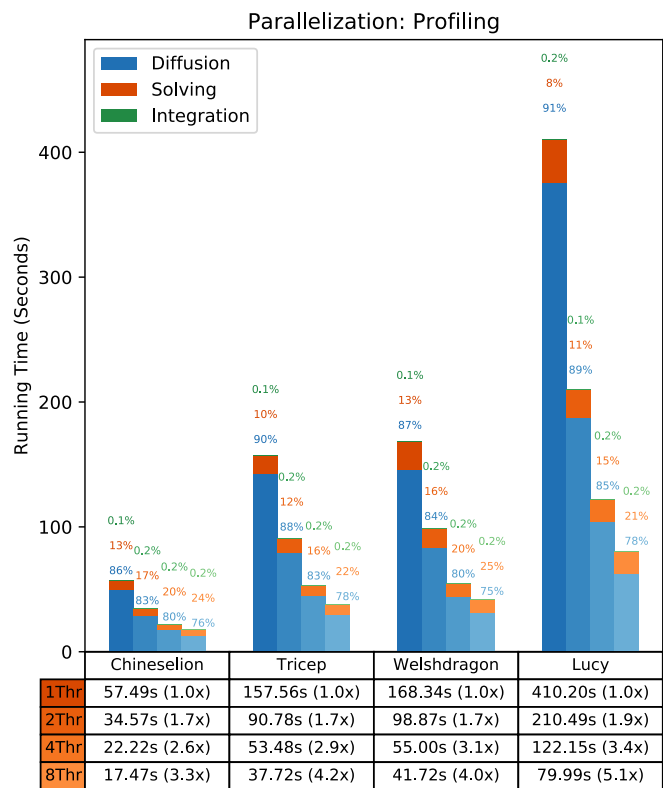


Fig. 10. We measure and visualize the timing for the three steps of our face-based method (heat diffusion (in blue), gradient optimization (in orange), and gradient integration (in green)), on different models using one, two, four and eight cores, respectively. All examples are tested with 600 Gauss-Seidel iterations and 10 ADMM iterations.

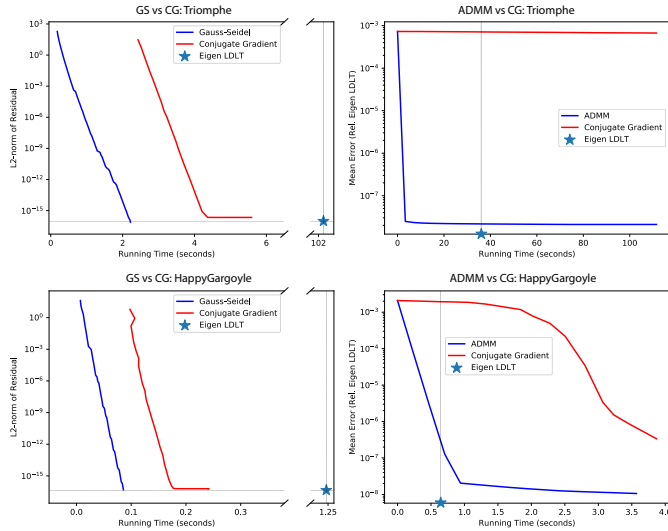


Fig. 11. Comparison between our face-based method and the original heat method using a conjugate gradient solver. The graphs show the change of solution accuracy with respect to computational time. The solution accuracy for the heat diffusion and the geodesic distance recovery is computed according to Eqs. (23) and (24) respectively.

5.4 Comparison with Iterative Linear Solver

The original heat method does not scale well because it adopts a direct linear solver that is known to have high memory footprints for large-scale problems. It is worth noting that the sparse linear systems in the original heat method can also be handled using iterative linear solvers with better memory efficiency for large problems. To evaluate the effectiveness of such approach compared with our methods, we replace the direct linear solver in the original heat method with the conjugate gradient (CG) method, a popular iterative solver for sparse positive definite linear systems. As the Poisson system in the heat method is only positive semi-definite, we fix the solution components at the source vertices to zero and reduce the system to a positive definite one that can be solved using CG. We adopt the CG solver from the EIGEN library [36] using the diagonal preconditioner. In Fig. 11, we show the relation between accuracy and computational time using the CG solver for heat diffusion and geodesic distance recovery, and compare it with our Gauss-Seidel (GS) heat diffusion and face-based ADMM gradient solver. For heat diffusion, we measure the accuracy of a solution \mathbf{u} using the ℓ_2 -norm of its residual with respect to the heat diffusion equation (3):

$$E_1(\mathbf{u}) = \|(\mathbf{A} - t\mathbf{L}_c)\mathbf{u} - \mathbf{u}_0\|_2. \quad (23)$$

For geodesic distance recovery, we measure the accuracy of a solution \mathbf{d} using the ℓ_2 -norm of its difference with the solution \mathbf{d}^* from a direct solver:

$$E_2(\mathbf{d}) = \frac{1}{n} \|\mathbf{d} - \mathbf{d}^*\|_2, \quad (24)$$

where n is the number of components in \mathbf{d} . We compute \mathbf{d}^* using the LDLT solver from EIGEN. For the ADMM solver, we integrate the resulting gradients according to Section 3.3 to obtain the solution \mathbf{d} . For reference, we also include the computational time and accuracy of the EIGEN LDLT solver in the comparison. Fig. 11 shows that both our GS heat diffusion and our ADMM gradient solver improves the accuracy faster than CG, making our approach a more suitable choice for handling large models.

5.5 Limitations

Similar to the original heat method, our method is also sensitive to the triangulation quality. The accuracy can be improved using Delaunay triangulation [37], but at the cost of increasing mesh complexity.

6 CONCLUSION & FUTURE WORK

In this paper, we develop a scalable approach to compute geodesic distance on mesh surfaces. Our method adopts a similar approach as the heat method, first approximating the geodesic distance gradients via heat diffusion, and then recovering the distance by integrated a corrected gradient field. Unlike the heat method which achieves this by solving two linear systems, we propose novel algorithms that can be easily parallelize and with fast convergence. The resulting method significantly outperforms the heat method while producing results with comparable accuracy. Moreover, its memory consumption grows linearly with respect to the mesh size, allowing it to handle much larger models. We perform extensive experiments to evaluate its speed, accuracy, and robustness. The results verify the efficiency and scalability of our method.

Our method can be improved in different aspects. First, although we only implement our method on CPUs using OpenMP, its massive parallelism allows it to be easily ported to GPUs, which we will leave as future work. Second, our algorithm is currently limited to meshes because of its reliance on a well-defined discrete gradient operator. As an extension, we would like to explore its application on other geometric representations such as point clouds and implicit surfaces. Finally, despite experiments showing that our formulation can handle surfaces of non-zero topology as well as multiple sources by only enforcing local compatibility of the gradients, we do not have a formal proof of this property. An interesting future research is to investigate how the accuracy of heat flow gradients affects the effectiveness of our formulation.

ACKNOWLEDGMENTS

The authors are supported by National Natural Science Foundation of China (No. 61672481), Youth Innovation Promotion Association CAS (No. 2018495), and Singapore MOE RG26/17.

REFERENCES

- [1] K. Crane, C. Weischedel, and M. Wardetzky, "The heat method for distance computation," *Commun. ACM*, vol. 60, no. 11, pp. 90–99, 2017.
- [2] G. Peyré, M. Péchaud, R. Keriven, and L. D. Cohen, "Geodesic methods in computer vision and graphics," *Foundations and Trends in Computer Graphics and Vision*, vol. 5, no. 3-4, pp. 197–397, 2010.
- [3] A. M. Bronstein, M. M. Bronstein, and R. Kimmel, "Three-dimensional face recognition," *International Journal of Computer Vision*, vol. 64, no. 1, pp. 5–30, 2005.
- [4] L. Najman and M. Schmitt, "Geodesic saliency of watershed contours and hierarchical segmentation," *IEEE Trans. Pattern Anal. Mach. Intell.*, vol. 18, no. 12, pp. 1163–1173, 1996.
- [5] N. Paragios and R. Deriche, "Geodesic active contours and level sets for the detection and tracking of moving objects," *IEEE Trans. Pattern Anal. Mach. Intell.*, vol. 22, no. 3, pp. 266–280, 2000.
- [6] W. Wang, J. Shen, R. Yang, and F. Porikli, "Saliency-aware video object segmentation," *IEEE Trans. Pattern Anal. Mach. Intell.*, vol. 40, no. 1, pp. 20–33, 2018.
- [7] D. Bryner, E. Klassen, H. Le, and A. Srivastava, "2d affine and projective shape analysis," *IEEE Trans. Pattern Anal. Mach. Intell.*, vol. 36, no. 5, pp. 998–1011, 2014.
- [8] G. Zigelman, R. Kimmel, and N. Kiryati, "Texture mapping using surface flattening via multidimensional scaling," *IEEE Trans. Vis. Comput. Graph.*, vol. 8, no. 2, pp. 198–207, 2002.

- [9] J. A. Sethian, *Level Set Methods and Fast Marching Methods: Evolving Interfaces in Computational Geometry, Fluid Mechanics, Computer Vision, and Materials Science*. Cambridge University Press, 1996.
- [10] —, “Fast marching methods,” *SIAM Review*, vol. 41, no. 2, pp. 199–235, 1999.
- [11] R. Kimmel and J. A. Sethian, “Computing geodesic paths on manifolds,” *Proceedings of the National Academy of Sciences*, vol. 95, no. 15, pp. 8431–8435, 1998.
- [12] J. S. Mitchell, D. M. Mount, and C. H. Papadimitriou, “The discrete geodesic problem,” *SIAM Journal on Computing*, vol. 16, no. 4, pp. 647–668, 1987.
- [13] J. Chen and Y. Han, “Shortest paths on a polyhedron,” in *Proceedings of the Sixth Annual Symposium on Computational Geometry*, ser. SCG ’90. New York, NY, USA: ACM, 1990, pp. 360–369.
- [14] K. Crane, C. Weischedel, and M. Wardetzky, “Geodesics in heat: A new approach to computing distance based on heat flow,” *ACM Trans. Graph.*, vol. 32, no. 5, pp. 152:1–152:11, 2013.
- [15] S. Varadhan, “On the behavior of the fundamental solution of the heat equation with variable coefficients,” *Communications on Pure and Applied Mathematics*, vol. 20, no. 2, pp. 431–455, 1967.
- [16] S. Boyd, N. Parikh, E. Chu, B. Peleato, and J. Eckstein, “Distributed optimization and statistical learning via the alternating direction method of multipliers,” *Found. Trends Mach. Learn.*, vol. 3, no. 1, pp. 1–122, 2011.
- [17] V. Surazhsky, T. Surazhsky, D. Kirsanov, S. J. Gortler, and H. Hoppe, “Fast exact and approximate geodesics on meshes,” *ACM Trans. Graph.*, vol. 24, no. 3, pp. 553–560, 2005.
- [18] S.-Q. Xin and G.-J. Wang, “Improving Chen and Han’s algorithm on the discrete geodesic problem,” *ACM Trans. Graph.*, vol. 28, no. 4, pp. 104:1–104:8, 2009.
- [19] X. Ying, X. Wang, and Y. He, “Saddle vertex graph (SVG): A novel solution to the discrete geodesic problem,” *ACM Transactions on Graphics*, vol. 32, no. 6, pp. 170:1–12, 2013.
- [20] X. Ying, S.-Q. Xin, and Y. He, “Parallel Chen-Han (PCH) algorithm for discrete geodesics,” *ACM Transactions on Graphics*, vol. 33, no. 1, pp. 9:1–9:11, 2014.
- [21] Y. Qin, X. Han, H. Yu, Y. Yu, and J. Zhang, “Fast and exact discrete geodesic computation based on triangle-oriented wavefront propagation,” *ACM Trans. Graph.*, vol. 35, no. 4, pp. 125:1–125:13, 2016.
- [22] O. Weber, Y. S. Devir, A. M. Bronstein, M. M. Bronstein, and R. Kimmel, “Parallel algorithms for approximation of distance maps on parametric surfaces,” *ACM Trans. Graph.*, vol. 27, no. 4, pp. 104:1–104:16, 2008.
- [23] A. G. Belyaev and P.-A. Fayolle, “On variational and pde-based distance function approximations,” *Computer Graphics Forum*, vol. 34, no. 8, pp. 104–118, 2015.
- [24] A. Greenbaum, C. Li, and H. Z. Chao, “Parallelizing preconditioned conjugate gradient algorithms,” *Computer Physics Communications*, vol. 53, no. 1, pp. 295–309, 1989.
- [25] M. Overby, G. E. Brown, J. Li, and R. Narain, “ADMM_∞ projective dynamics: Fast simulation of hyperelastic models with dynamic constraints,” *IEEE Transactions on Visualization and Computer Graphics*, vol. 23, no. 10, pp. 2222–2234, 2017.
- [26] Y. Wang, J. Yang, W. Yin, and Y. Zhang, “A new alternating minimization algorithm for total variation image reconstruction,” *SIAM J. Imaging Sciences*, vol. 1, no. 3, pp. 248–272, 2008.
- [27] M. K. Ng, P. Weiss, and X. Yuan, “Solving constrained total-variation image restoration and reconstruction problems via alternating direction methods,” *SIAM J. Scientific Computing*, vol. 32, no. 5, pp. 2710–2736, 2010.
- [28] L. Xu, C. Lu, Y. Xu, and J. Jia, “Image smoothing via L_0 gradient minimization,” *ACM Trans. Graph.*, vol. 30, no. 6, pp. 174:1–174:12, 2011.
- [29] F. Heide, S. Diamond, M. Nießner, J. Ragan-Kelley, W. Heidrich, and G. Wetzstein, “Proximal: efficient image optimization using proximal algorithms,” *ACM Trans. Graph.*, vol. 35, no. 4, pp. 84:1–84:15, 2016.
- [30] K. Crane, M. Desbrun, and P. Schröder, “Trivial connections on discrete surfaces,” *Computer Graphics Forum*, vol. 29, no. 5, pp. 1525–1533, 2010.
- [31] D. Eppstein, “Dynamic generators of topologically embedded graphs,” in *Proceedings of the Fourteenth Annual ACM-SIAM Symposium on Discrete Algorithms*, ser. SODA ’03, 2003, pp. 599–608.
- [32] S. Campagna, L. Kobbelt, and H.-P. Seidel, “Directed edges—a scalable representation for triangle meshes,” *J. Graph. Tools*, vol. 3, no. 4, pp. 1–11, 1998.
- [33] L. Kettner, “Using generic programming for designing a data structure for polyhedral surfaces,” *Computational Geometry*, vol. 13, no. 1, pp. 65–90, 1999.
- [34] HSL, “A collection of fortran codes for large scale scientific computation,” 2018.
- [35] J. D. Hogg, J. K. Reid, and J. A. Scott, “Design of a multicore sparse cholesky factorization using dags,” *SIAM J. Sci. Comput.*, vol. 32, no. 6, pp. 3627–3649, 2010.
- [36] G. Guennebaud, B. Jacob *et al.*, “Eigen v3,” <http://eigen.tuxfamily.org>, 2010.
- [37] Y. Liu, C. Xu, D. Fan, and Y. He, “Efficient construction and simplification of delaunay meshes,” *ACM Trans. Graph.*, vol. 34, no. 6, pp. 174:1–174:13, 2015.